Segmentation and Tracking of Migrating Cells in Videomicroscopy With Parametric Active Contours: A Tool for Cell-Based Drug Testing

Christophe Zimmer*, Elisabeth Labruyère, Vannary Meas-Yedid, Nancy Guillén, and Jean-Christophe Olivo-Marin

***Abstract*—This paper presents a segmentation and tracking method for quantitative analysis of cell dynamics from *in vitro* videomicroscopy data. The method is based on parametric active contours and includes several adaptations that address important difficulties of cellular imaging, particularly the presence of low-contrast boundary deformations known as pseudopods, and the occurence of multiple contacts between cells. First, we use an edge map based on the average intensity dispersion that takes advantage of relative background homogeneity to facilitate the detection of both pseudopods and interfaces between adjacent cells. Second, we introduce a repulsive interaction between contours that allows correct segmentation of objects in contact and overcomes the shortcomings of previously reported techniques to enforce contour separation. Our tracking technique was validated on a realistic data set by comparison with a manually defined ground-truth and was successfully applied to study the motility of amoebae in a biological research project.**

***Index Terms*—Active contours, cellular imaging, pseudopods, quantitative cellular models, repulsion, segmentation, topology changes, tracking, video-microscopy.**

I. Introduction

A. Cell Dynamics and Image Analysis

CELL dynamics is a crucial aspect of many biological processes with direct implications for human health. Cell motion is essential, for instance, in tumor metastasis, wound repair, and host invasion by parasites [1], [2]. Changes in cellular morphology also play a critical role in the recognition by immune cells of antigens at the "immune synapse" [3], or the phagocytosis of host cells by parasites. An important effort of drug development therefore aims to alter the dynamic properties of cells, e.g., by inhibiting the motility of a parasite.

To reliably assess the clinical potential of candidate drugs, it is usually necessary to analyze quantitatively the motion and morphology changes of a large number of cells under a variety of experimental conditions. Recent advances in light microscopy have facilitated the observation of the dynamics of living cells during extended periods of time. The increasing quantity and complexity of image data from dynamic microscopy renders manual analysis (already prone to errors due to user bias and lack of reproducibility) unreasonably time-consuming, if not impossible. Therefore, automatic techniques to extract cellular motion and morphology characteristics from image sequences are of considerable interest to exploit microscopy data in the drug discovery process.

In this paper, we present such a technique, motivated by the desire to study the kinetic properties of the motile microorganizm *Entamoeba histolytica*, a unicellular parasite responsible for invasive amoebiasis, which causes 100 000 deaths/year. Our goal is to establish a platform to analyze quantitatively the motion and shape changes of *E. histolytica* cells, which are essential factors for its virulence. This requires the ability to segment and track biological cells in large image sequences acquired by optical video-microscopy. Our method is designed to produce an accurate description of the outlines of each cell in every image (segmentation step), and to keep track of the cell identities across the sequence (tracking step). The extracted data can be used straightforwardly to compute quantitative parameters characterising cellular motion and morphology.

B. Segmentation and Tracking of Cells

While a large body of work has addressed the segmentation and tracking of medical images on the scale of individual organs (e.g., [4] and [5]), relatively little effort has been devoted to cellular imaging. Some of these efforts have used model-free segmentation methods such as thresholding of the gradient image [6], [7], combined with tracking algorithms that pair detected objects from consecutive frames in a sequence. Methods of this type have been used with success to study the motion of isolated cells [7], [8]. However, they provide no or only poor descriptions of the cellular shape. In fact, they usually do not even produce closed-object contours and require important post-processing steps to obtain those. In addition, these approaches often fail to correctly track multiple cells in sequences exhibiting cell-cell contacts [6].

Some of these difficulties can be avoided by using model-based techniques such as active contours (or "snakes") [9]. Active contour methods automatically produce closed and smooth object boundaries, and offer the possibility of providing a first guess through the interactive initialization step. Provided that

Manuscript received October 31, 2001; revised August 13, 2002. This work was supported by the Institut Pasteur and INSERM. The work of C. Zimmer was funded through a "Programme Transversal de Recherche" fellowship from Institut Pasteur. *Asterisk indicates corresponding author.*

*C. Zimmer is with the Quantitative Image Analysis Unit, Institut Pasteur, and also with the CNRS UMR 1947, 75724 Paris, France (e-mail: czimmer@pasteur.fr).

E. Labruyère and N. Guillén are with the Cell Biology of Parasitism Unit, Institut Pasteur, and also with the INSERM U-389, 75724 Paris, France.

V. Meas-Yedid and J.-C. Olivo-Marin are with the Quantitative Image Analysis Unit, Institut Pasteur, and also with the CNRS UMR 1947, 75724 Paris, France.

Digital Object Identifier 10.1109/TMI.2002.806292

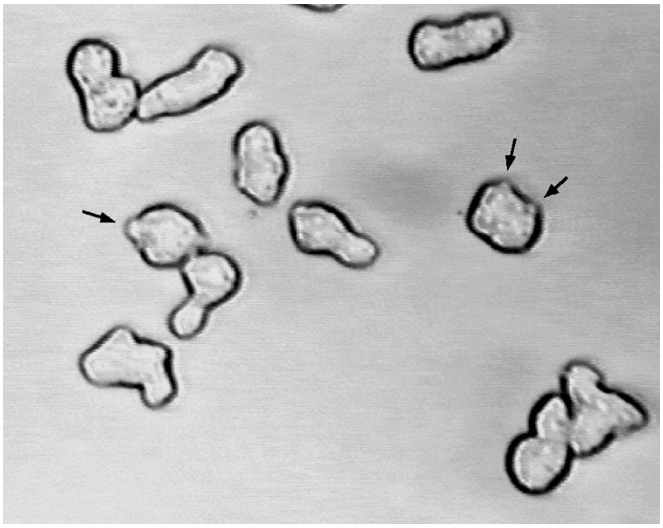

Fig. 1. Typical image of *E. histolytica* cells observed under a phase contrast microscope (fragment). Arrows point at some pseudopods. The field of view is roughly 300×250 μm and the image size is 460×380 pixels.

the temporal resolution is sufficient, they also allow to keep track of object identity in an obvious manner through automatic initialization based on the segmentation of the previous image. Leymarie and Levine [10] demonstrated that an active contour method can track the membrane of single fibroblast cells through a sequence of images from light transmission microscopy. Giuliano *et al.* [11] have used a similar method to track the motion and deformation of spatially isolated tumor cells, and a first application of active contours to the tracking of isolated *E. histolytica* cells was presented in [12].

C. This Work

The images under consideration in our paper (see example in Fig. 1), present two main difficulties that significantly limit the applicability of the previous methods: the presence and importance of pseudopods, and the propensity of cells to divide and adhere to each other.

Pseudopods are transient protrusions of the cellular membrane used for locomotion and phagocytosis, and are therefore important to detect correctly in motility and morphology studies. Because they are generally partly or entirely localized outside of the focal plane, these features appear at much lower contrast than most of the cell membrane, and tend to be treated by snakes as occlusions, i.e., ignored, as already deplored by [10]. In wild-type amoebae, pseudopods tend to grow and the whole cell subsequently moves in the direction of the pseudopod. As a result, failure to detect a pseudopod in one frame will lead to an initial contour increasingly distant from the deformed cell membrane in the following frames. Thus, even if the contrast of the boundary deformation later increases, the snake may be too far from the actual cell boundary to produce a correct segmentation. The snake then tends to collapse under the influence of its internal tension, ultimately leading to a complete breakdown of segmentation and tracking (see [13]). In Section III, we will describe a scheme designed to enhance the detection of pseudopods by active contours.

Contacts between cells are another important difficulty of our data and cellular imaging in general. Since the dynamic behavior of motile cells is strongly influenced by the interactions with other cells [14], these interactions cannot be avoided in *in vitro* experiments designed to reflect *in vivo* conditions. However, object contacts pose a significant challenge to active contour methods, as a snake associated to one object may easily be attracted to parts of a neighboring object, again leading to a breakdown of segmentation and tracking. In Section IV, we will discuss this problem in detail and describe a new method to handle cell contacts.

In Section II, we recall the original snake model [9], as well as a useful and popular extension, the "GVF" model [15], and discuss their applicability to our data. In Section V, we compare the results obtained by our method with a manually defined ground-truth and briefly present an application of our method to the study of amoebic motility. We conclude (Section VI) with a short summary and outlook on future work.

II. Parametric Active Contour Models

A. Original Model

The parametric active contour (or "snake") model first introduced by [9] consists in minimizing the energy functional $E(\mathbf{C})$ of a curve $\mathbf{C}(s) = (x(s), y(s))$ parameterized by $s \in [0,1]$, with

$$E(\mathbf{C}) = \int_0^1 \left(\frac{1}{2} \left[\alpha \left| \mathbf{C}_s \right|^2 + \beta \left| \mathbf{C}_{ss} \right|^2 \right] - f\left(\mathbf{C}(s)\right) \right) ds. \quad (1)$$

Here, α and β are scalar coefficients, subscripts denote partial derivatives, and f is an edge map of the image. An appropriate choice for f in images where object boundaries are dark, such as Fig. 1, is $f = -G_\sigma * I$, where I is the image intensity, G_σ is a Gaussian kernel and $*$ denotes convolution. The minimization of the terms inside brackets, called the internal energy, which depend only on the geometry of the curve, tends to enforce a certain smoothness and acts as a regularising constraint helping to overcome image noise. The minimization of the last term, called the external energy, tends to push the curve toward object edges (where f is large). In practice, the minimization of E is performed iteratively by considering the curve as a function $\mathbf{C}(s,t)$ of an abstract time t. Starting from an initial guess $\mathbf{C}(t=0) = \mathbf{C_0}$, the curve is deformed according to the evolution equation

$$\mathbf{C}_t = \alpha \mathbf{C}_{ss} - \beta \mathbf{C}_{ssss} + \nabla f \quad (2)$$

until it reaches an equilibrium. Following a standard terminology, we will refer to the terms on the right hand side of (2) as forces. At equilibrium, (2) reduces to the Euler–Lagrange equation associated to a local minimization of E.

Because the minimization is local, the equilibrium position of the curve usually depends on the initialization $\mathbf{C_0}$. In the original model, the external image-driven force [last term of (2)] is significant only in the immediate vicinity of the object boundaries. Elsewhere, the snake's evolution is driven dominantly by the internal forces [first two terms of (2)], which lead to shrinking and smoothing of the contour. As a result, the

original model requires an initial guess close to the actual object boundaries, or at least located outside of the object, so that the shrinking forces move the contours close to the boundaries where the external force becomes important.

In processing temporal sequences, the initialization of the active contours can easily be done manually on the first frame of the sequence, but should be automatic for the rest of the sequence. Because cells move relatively little between consecutive frames, a good initial guess of the contour location is provided by the final contour of the previous frame, thus allowing a straightforward automatic initialization that trivially links object positions across frames. With such a scheme, however, the initial contour is generally not located outside of the object, nor is it always sufficiently close to its boundaries, so that the original snake model usually fails [13]. In addition, as mentioned in the introduction, even when most of a cell's boundary is correctly segmented, the original snake model is usually unable to correctly locate the small low contrast membrane deformations due to pseudopods. We therefore adopted the gradient vector flow (GVF) model of [15] designed both to reduce the sensitivity of the snake to initial conditions, and to increase segmentation performance on boundary concavities.

B. GVF Model

In the GVF model [15], the external force ∇f in (2) is replaced by a new vector field $\mathbf{v}$, which is defined as the steady-state solution of the following reaction-diffusion equations:

$$\mathbf{v}_t = \mu\nabla^2\mathbf{v} - (\mathbf{v} - \nabla f)\,|\nabla f|^2\,; \qquad \mathbf{v}(t=0) = \nabla f. \quad (3)$$

Near object boundaries, where $|\nabla f|$ is large and the reaction term (last term in (3)) dominates, the GVF model leaves the external force field approximately unchanged from its original value: $\mathbf{v} \approx \nabla f$. Elsewhere in the image, the diffusion process [first term on the right-hand side of (3)] dominates, thus, noise is reduced and the resulting field $\mathbf{v}$ is "interpolated" from ∇f between the object boundaries. Because the information from strong object boundaries is propagated throughout the image by the diffusion process, the GVF model enjoys a much larger "capture range" than the original snake model and is considerably less sensitive to initialization. This is also the case in our data, where thanks to the GVF, contours can converge toward the objects even with a much cruder initialization.

However, although the GVF model was proven to be superior in detecting concave boundaries [15], it does not solve the difficulties posed by less pronounced boundary deformations such as the pseudopods. In fact, the GVF even exacerbates these difficulties; as we pointed out recently [13], the diffusion process of (3) leads to a competition of boundaries, in the course of which the influence of image features with large edge map gradient $|\nabla f|$, i.e., the stronger boundaries, progressively overwhelms the influence of weaker boundaries. This can lead to incorrect segmentations by the GVF even in cases where the initial contour is positioned at the object boundary itself and the original model [9] succeeds (see [13, Figs. 6 and 7]). This undesired effect of boundary competition can be reduced by halting the diffusion process (3) before it reaches a steady–state. Although this modification moderates the domination of strong edges, it alone cannot render weak edges more attractive than in the original model [9] itself. To achieve detection of pseudopods within the framework of GVF snakes, the edge map must be enhanced at weak boundary portions. Section III describes a dedicated technique to do this.

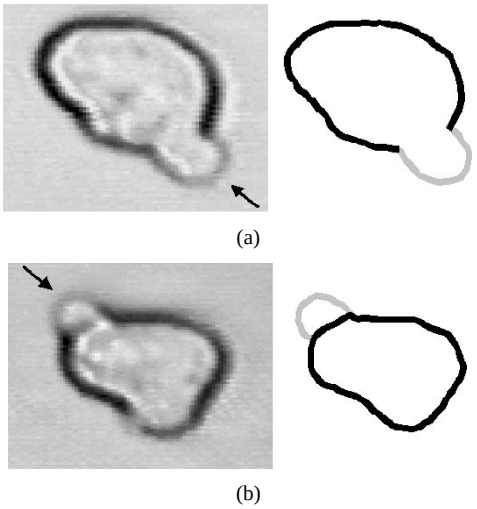

Fig. 2. Two types of pseudopods (arrows). (a) "Continuous membrane" type. (b) "Graft" type.

III. Enhancing Detection of Low Contrast Boundaries

The difficulty in detecting pseudopods stems from the fact that they cannot be distinguished on the basis of their grey-level or gradient values alone from features visible inside the cells such as vesicles (see Figs. 1 and 2). To address this problem, we previously [13] used a hysteresis thresholding of the Canny [16] edge map, followed by binarization. The hysteresis thresholding helps to discriminate pseudopods against intracellular features based on their connectivity with the high-contrast part of the cellular membrane, and the binarization then gives pseudopods the same strength in the edge map as the high-contrast portions. This considerably improves the detection of pseudopods appearing as low contrast portions of an otherwise high-contrast membrane [Fig. 2(a)]. However, the method fails in the frequent cases where the pseudopod extends predominantly out of the focal plane. In this case, the pseudopod appears as a "graft" on the high contrast membrane rather than a continuation of it [Fig. 2(b)]. This type of feature is unlikely to be correctly segmented by our previous approach [13], or by any purely edge-based approach, since the high contrast boundary will qualify as an edge at least to the same degree, if not more, than the low contrast pseudopod.

In this paper, in contrast, we propose a modification of the edge map f intended to facilitate the detection of weak object boundaries on the basis of their proximity to pixels of the background. This approach is made possible by the relative homogeneity of the substrate in *in vitro* microscopy. After testing a number of texture parameters, we found that the local average deviation I_{AD} is particularly suited to distinguish background pixels from object and boundary pixels

$$I_{AD}(i_0, j_0) = \frac{1}{(2M+1)^2} \sum_{(k,l)\in[-M,M]^2} \left| I\,(i_0 + k, j_0 + l) - \bar{I} \right|$$

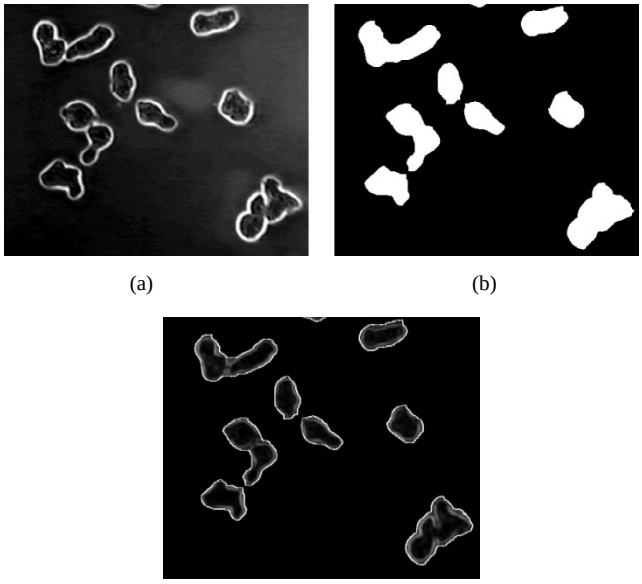

(a) (b)

(c)

Fig. 3. (a) Original edge map $f = -G_\sigma * I$ of the image in Fig. 1. (b) Binary object mask I_{OM} obtained by a seed flood on the average deviation I_{AD} of Fig. 1. Note that cells in contact are not separated. (c) New edge map f_2. Note that bright contours along cell boundaries, including pseudopods, clearly stand out, while the boundaries between cells in contact are still visible.

where $I(i,j)$ is the intensity at pixel (i,j), and $\bar{I}$ is the mean intensity

$$\bar{I} = \frac{1}{(2M+1)^2} \sum_{(k,l)\in[-M,M]^2} I\left(i_0+k, j_0+l\right)$$

over square windows of size $2M+1$, with, e.g., $M=3$. A simple thresholding of the average deviation image easily eliminates the background, but may also eliminate regions inside the cell. We, therefore, prefer to perform a seed flood, starting from the image borders, on the average deviation image I_{AD} of pixels with grey levels below a certain threshold I_{th} (we used $I_{th}=3$). If all I_{AD} pixels of the object boundary have intensities above I_{th}, as often is the case, then nonflooded regions form closed objects that correspond either to a single cell or to an agglomeration of cells. Binarization of the flooded image yields a mask I_{OM} [Fig. 3(b)] consisting of regions, whose boundaries are then readily obtained as a binary image f_B. The nonzero pixels of f_B are a good indication of cell-background interfaces (compare Figs. 3(b) and 1), and are, therefore, of great value for the localization of pseudopods.

Unfortunately, for cells in contact, any boundary visible between the cells on the original image is lost in I_{OM} [as evident from Fig. 3(b)] and consequently also in f_B. Furthermore, the seed flood of I_{AD} may occasionally "leak" through particularly fuzzy membranes, yielding parasitic boundaries inside the objects at locations where no such boundaries exist in the original image (not shown). For these two reasons, we chose to reintroduce some amount of information from the grey-level image I_{AD} by linearly combining f_B and I_{AD} masked by I_{OM}

$$f_2 = (I_{AD} \wedge I_{OM}) + \lambda f_B.$$

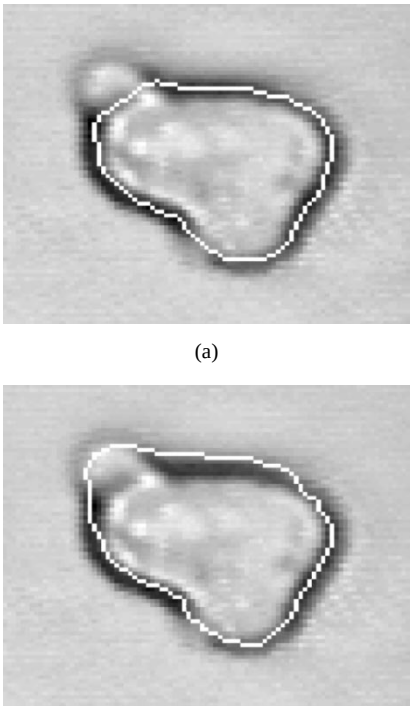

(a)

(b)

Fig. 4. Segmentation of the "graft type" pseudopod of Fig. 2(b). (a) Using the original edge map f. (b) Using the edge map f_2 of Section III.

Here, f_2 designates the new edge map, I_{AD} and f_B are normalized to the range [0, 1], and λ is a scalar parameter weighting the importance of the object/background boundaries relative to the original edge map (we used $\lambda = 2$). The new edge map exhibits the desired properties of having high intensity pixels at the boundaries of cells on the background, while having smaller, but still significant, intensities at boundaries between cells in contact [see Fig. 3(c)]. This makes f_2 a better choice than the original edge map f [Fig. 3(a)] for the detection of pseudopods and an equally good choice for the detection of intercellular boundaries.

Our new edge map is now used in the snake and GVF model previously described (simply replace f by f_2 in Section II). Thanks to this change, an accurate segmentation of cell shapes including pseudopods is now possible [see Fig. 4(b)], thus allowing detailed studies of the morphological changes of these highly deformable cells.

IV. Handling Cell Interactions With Repulsive Contours

A. Parametric Versus Level-Set Contours

As we noted in the introduction, cells are likely to interact closely with each other and undergo divisions. These situations cannot be handled with traditional parametric active contours. When two cells approach each other, their associated snakes are likely to be attracted to parts of the other cell, while also remaining attached to their legitimate object (see [13, Fig. 13]). Similarly, when a cell divides and the daughter cells separate, the snake remains attached to both objects. The inability of parametric contours to handle cell interactions is due to the independent application of a single-object model to the different objects

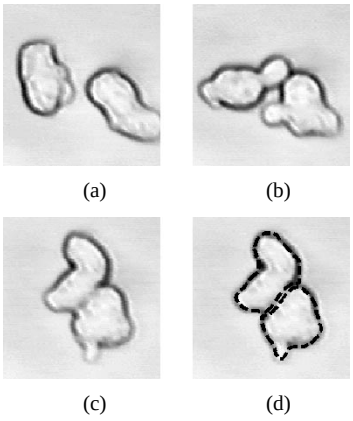

Fig. 5. Two amoeba have come in close contact (a-c). A level-set technique would identify the cell compound in (c) as a single object, even if two objects were detected in (a) and (b). (d) Parametric methods however maintain two distinct contours (result obtained with the method described in this paper).

in the image, i.e., to the absence of coupling between contours. The failure to handle cell divisions stems from the topological rigidity of parametric models.

In recent years, a segmentation approach based on level-set methods [17] has become increasingly popular (e.g., [18] and [19]), partly because it is able to overcome both of these shortcomings. In these methods, contours are defined implicitly as the zero level set of an evolving surface and thus do not require any explicit parametrization and do not suffer from any constraints on the topology. They also produce closed contours, while allowing the number of these contours to adapt to the number of objects in the image.

The level-set approach would thus seem to be a more appropriate framework for cell segmentation than traditional parametric methods. However, the topological flexibility of level sets has a significant drawback in cellular imaging. In many cases, previously distant cells [as in Fig. 5(a)] later enter into close interactions that blur the boundary between them, which becomes less pronounced than the cell-background boundary [Fig. 5(c)]. In these cases, a level-set method will merge the two contours into a single object. Cell fusions, however, are biologically impossible in our (and in most) biological contexts. It is therefore desirable to constrain the topology changes in such a way as to prevent fusion of contours. It is not clear how this could be done within the level-set framework. In contrast, it is possible within the parametric approach to separate objects in contact by prohibiting contour fusions, while allowing automatic object divisions. This was demonstrated most recently by the technique of [20], which we discuss in the following.

B. Topological Operators

The technique of 'topological operators' proposed by [20] extends the framework of parametric active contours by 1) allowing contours to split if their deformation leads to a "bottleneck" geometry (see [20, Fig. 24]), and 2) keeping contours separated by removing overlapping snake areas (see [20, Fig. 14]). Both tasks use an efficient grid-based algorithm to detect contour intersections and can be performed whenever required during the contour deformation process described in Section II-A.

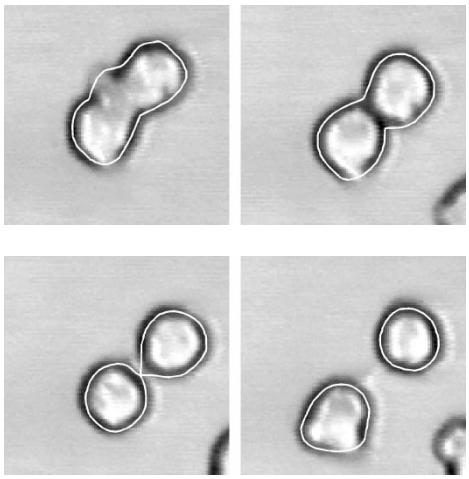

Fig. 6. Automatic splitting of the contour associated to a dividing amoeba, using topological operators [20].

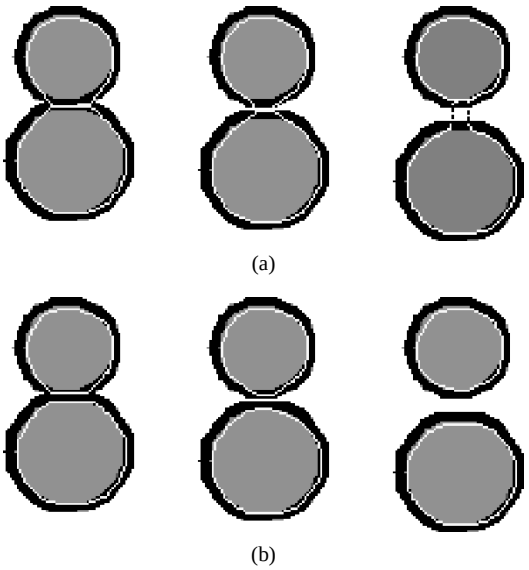

Fig. 7. Keeping snakes separate when objects in contact move away from each other. The three frames are processed as a sequence, from left to right. (a) Using topological operators [20]; note the incomplete separation of the lower snake from the upper object. (b) Using intersnake repulsion (Section IV-C).

The ability to split contours allows to automatically handle the topological change of a dividing cell and independently track the two daughter cells, as illustrated in Fig. 6.

The ability to restore contour separations by removing overlaps is useful for objects in contact [20], [13], as this procedure reduces the likelihood that contours converge toward the boundaries of other object (see [13, Fig. 14]).

Unfortunately, though, this method does not guarantee that the separation of contours occurs at the desired location, namely the actual interface between objects. When two objects initially in contact move away from each other, at least one of the snakes is likely to remain attached to the other object, even though the two snakes do not strictly overlap [see Fig. 7(a)]. This undesired behavior stems from the fact that the motion of snakes is independent of the other snakes as long as they do not overlap; on the other hand, when the snakes do overlap, their boundaries are modified based solely on the relative contour geometry, thus

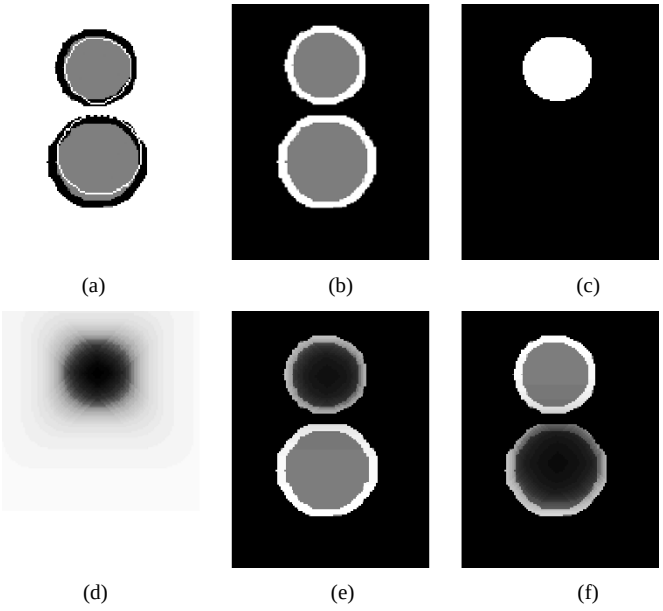

Fig. 8. Modified edge map and its intermediaries. (a) Synthetic image of Fig. 7 (third and last frame) and the initial contours obtained from the segmentation of the middle frame in Fig. 7(b). (b) Original edge map $f = -I$. (c) Object mask I_{OS} associated to the top snake of (a) (the neighbor of the bottom snake). (d) Modulation image I_{mod} for the bottom snake. (e) Modified edge map f_3 for the bottom snake. (f) Modified edge map f_3 for the top snake.

ignoring all information from the image. In order to simultaneously prevent contours from crossing each other and move neighboring contours toward actual boundaries on the image, it, therefore, seems desirable to integrate in the same process the requirement of object separation and the image-driven deformation scheme.

C. Repulsive Contours

While contours previously evolved independently of each other, under the sole influence of their own geometry and of the image, we now wish to integrate a repulsive interaction between contours into the evolution process. This can be achieved effectively by a modification of the edge map for each contour, as we describe next.

In our approach, contours are allowed to move simultaneously (i.e., all snakes are processed at each iteration of the discretization of (2) in Section II-A). For each snake $\mathbf{C}$ [for example, the bottom snake in Fig. 8(a)], we define the "neighbor snakes" as all other snakes present in a local window centered on the initial contour $\mathbf{C_0}$ [in this example, the only neighbor snake is the top snake in Fig. 8(a)]. The local window needs only be chosen large enough to make sure that it contains the new position of the object. We then construct a binary object mask I_{OS} from the regions enclosed by the neighbor snakes [see Fig. 8(c)]. Next, we compute the algebraic distance map I_D associated to I_{OS}, with positive values outside the snakes, and negative values inside (not shown). We now apply to I_D the function

$$g(r) = \frac{1}{2} + \pi^{-1} \tan^{-1}\left(\frac{r}{r_0}\right)$$

plotted in Fig. 9, which results in what we call the "modulation image" $I_{\mathrm{mod}} = g(I_D)$ [see Fig. 8(d)]. The modulation image

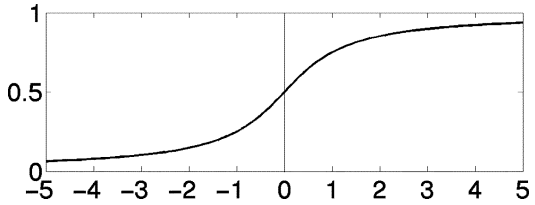

Fig. 9. Modulation function g used to attenuate the edge map at the vicinity and inside neighboring snakes.

has pixel values close to 1 at locations that are distant by more than r_0 pixels from the neighbor snakes, and values close to zero at locations at least r_0 pixels deep inside these snakes. (For $r_0 \to 0$, I_{mod} reduces to the complement of the binary image I_{OS}). Finally, we multiply the original image edge map (for the synthetic data shown here we use $f = -I$, see Fig. 8(b); for the real data we use f_2 from Section III) by the modulation image I_{mod}. This results in f_3 [see Fig. 8(e)], which can be described as a "context sensitive" edge map attached to snake $\mathbf{C}$.

This new edge map f_3 is approximately identical to the original edge map [Fig. 8(b)] at distances $r > r_0$ from the neighbor snakes, but increasingly attenuated from the original edge map as one approaches the neighbor snakes, and is almost zero at depths $r > r_0$ inside these snakes. Consequently, edges located inside or in the immediate vicinity of the neighbor snakes are made less attractive for snake $\mathbf{C}$, which is thus encouraged to move instead toward edges located outside of the neighbor snakes. A context-sensitive edge map f_3 is constructed in the same manner for each neighbor snake [see Fig. 8(f)], and this edge map penalises motion toward snake $\mathbf{C}$. As a result, snakes now experience a repulsion from other snakes, even if they are not in actual contact. This effective "buffer zone" between snakes helps to correctly dissociate contours when two objects in contact move away from each other, as shown in Fig. 7(b). The width of the buffer zone (or the range of the "repulsion force") in pixels is of the order of r_0. This parameter should be set according to the possible displacement of object boundaries between consecutive frames. For both the real data analyzed in this paper and the synthetic images of Figs. 7 and 8, we used $r_0 = 5$.

Our repulsive contour approach places no restrictions on the number of snakes in the image and does not suffer from increased complexity in the case of multiple objects, in contrast to the topological operators [20], whose generalization to more than two objects in contact poses significant difficulties. However, because the modified edge map f_3 is snake dependent, it must be recomputed for each individual object. Although this significantly increases the processing load, the added benefit is well worth the additional cost in this applicative context where constraints on computation time are relatively low.

V. Results

A. Summary of the Presented Method

The practical implementation of our method for cell segmentation and tracking can be summarized as follows: for each image, we first construct the edge map f_2 based on the local average deviation, as described in Section III. Then, for each initial contour $\mathbf{C_0}$ present in the image, we compute the context-sensitive edge map f_3 by modulating f_2, as detailed

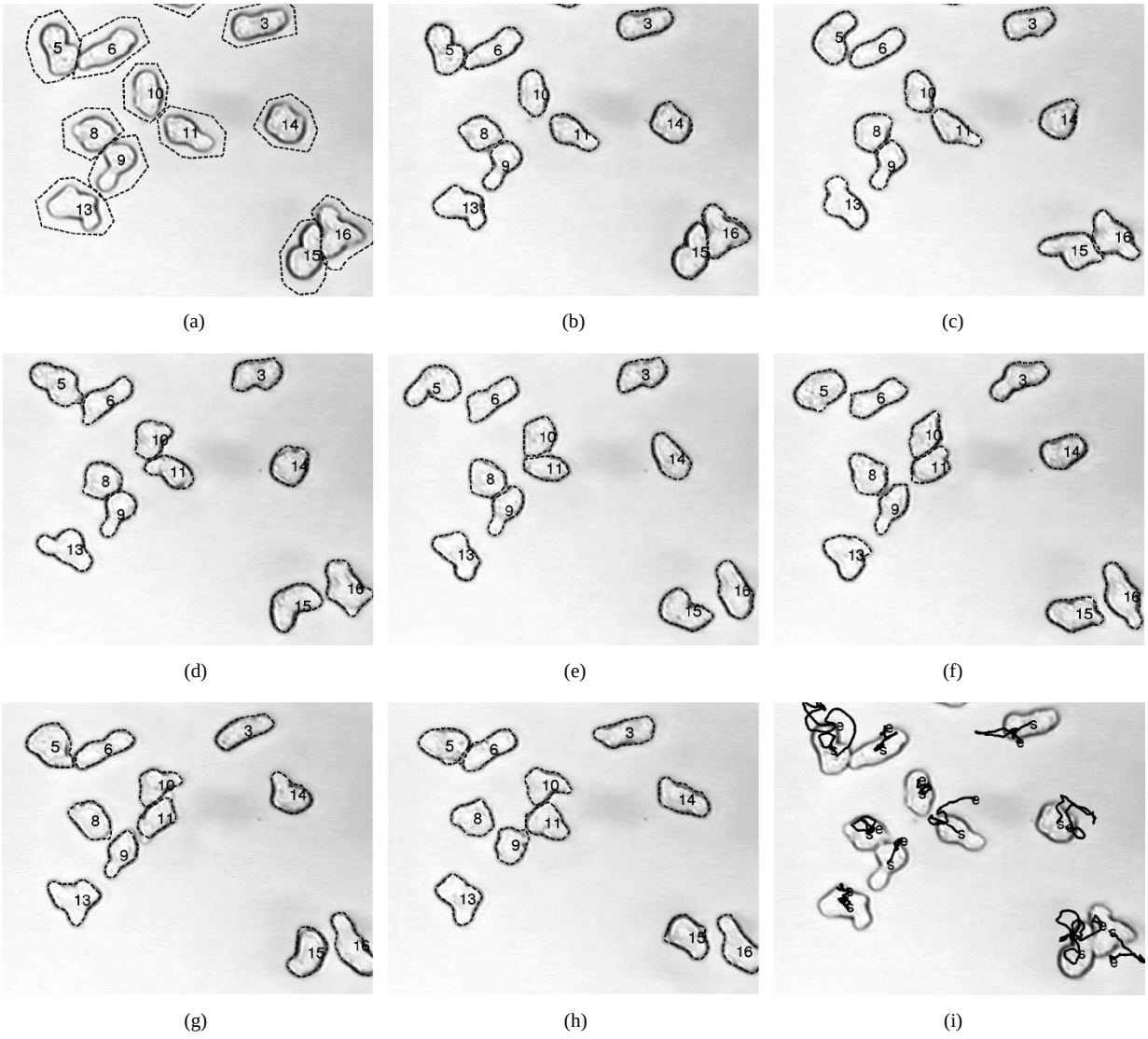

Fig. 10. Segmentation and tracking of motile cells observed during a 1-min time sequence starting with Fig. 1. (a) Initialization at $t = 0$ s. (b-h) Segmentation results at $t = 0$ s, 10 s, 20 s, 30 s, 40 s, 50 s, and 60 s. (i) Cell trajectories (during 5 min) superimposed on the first frame. Processing was done on frames separated by intervals of 1 s.

in Section IV-C. Next, the GVF field $\mathbf{v}$ for $\mathbf{C_0}$ is computed from (3), where f is replaced by f_3. Finally, the contours are moved according to (2), where ∇f is replaced by $\mathbf{v}$. To limit processing time, all contour-specific quantities, such as f_3 and $\mathbf{v}$, are computed only in local windows centered on the considered contours.

The initial contours are defined manually as polygons enclosing each individual cell on the first image of each temporal sequence, as in Fig. 10(a). To allow for such a crude initialization and force the convergence of contours toward the cells that are inside the initial polygons, we set the edge map f_2 to zero outside these polygons; this is done for the first frame only. For all following frames, the initial contours are obtained from the detected contours of the previous frame, thus, automatically linking objects across frames.

Fig. 10 illustrates a successful application of our method to the segmentation and tracking of motile cells moving by pseudopod extensions and undergoing frequent intercellular contacts. A more systematic evaluation of our technique is presented in the following.

B. Validation of Automatic Cell Tracking

In this section, we describe experimental assessments of our method's benefits by comparing it with both previous approaches based on parametric active contours and manually obtained tracking results.

Our trial data consist of six image sequences obtained from phase contrast videomicroscopy, totalling nearly 2000 frames. To confront the key difficulties addressed in this paper, we chose image sequences in which many cells moved appreciably (i.e., over distance at least comparable to their diameter) and frequently interacted with each other (see Fig. 11). We confined our analysis to cells entirely contained in the image during the whole sequence (hereafter called "target cells"), thus, ignoring cells that left from or appeared in the field of view in the course of the sequence, both situations that our method is not yet designed to address. The total number of target cells in our data set is 84. In all tests, we monitored the surface of the segmented cells in each frame and terminated tracking for cells whose computed surface reached unreasonably small or large values. A

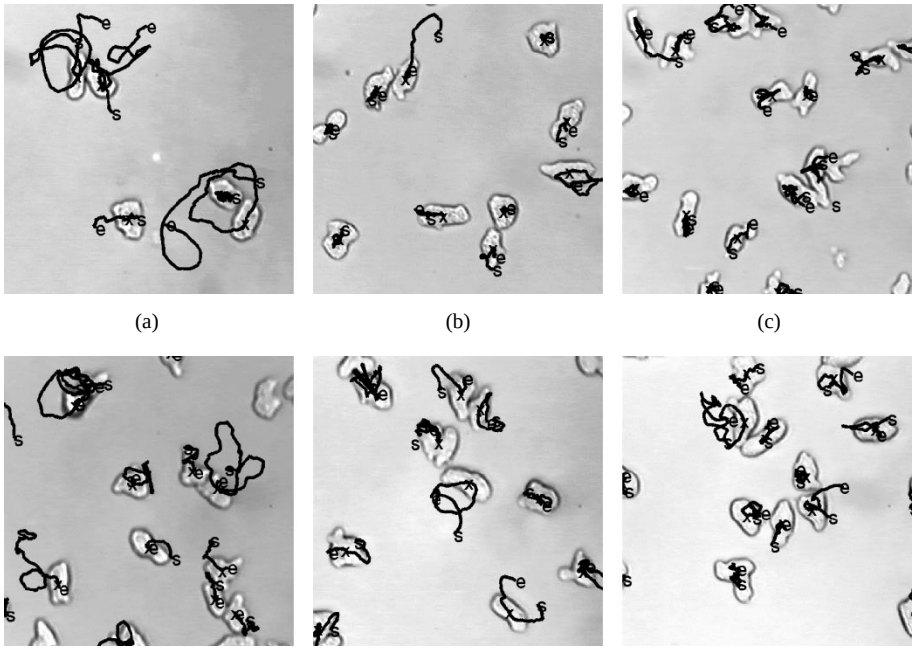

Fig. 11. Cell tracking on the six trial sequences. One representative image fragment is shown from each sequence, together with the computed cell trajectories. The start and end points of each trajectory are marked "s" and "e," respectively. Positions of cells in the displayed frame are marked with "x." The number of frames and "target" cells (see text) for each sequence are as follows: (a) 540 frames, 7 cells; (b) 300 frames, 10 cells; (c) 300 frames, 16 cells; (d) 300 frames, 22 cells; (e) 150 frames, 14 cells; and (f) 300 frames, 15 cells. The time interval between consecutive frames in each sequence is 1 s.

useful indicator of the method's robustness is thus provided by the number of cells tracked without termination through the entire sequence divided by the total number of target cells. We will refer to this ratio as "tracking performance." In order to demonstrate the improvements in tracking obtained by the approach proposed here, we tested the following three methods:

- the GVF active contour model [9], [15] with the standard edge map $f = -G_\sigma * I$ (method KX);
- our previous method detailed in [13], which uses Canny edge filtering and hysteresis thresholding to enhance pseudopod detection and relies on topological operators [20] to enforce contour separations (method Z01);
- the method described in this paper (method Z02).

Table I indicates the tracking performances achieved by the three methods on each trial sequence (a)–(f). The average tracking performance of the method Z02 proposed here, as estimated on our trial data, is 95%, compared to 67% for our previous method Z01 [13] and 45% for the original GVF snakes of method KX [9], [15] (Table I, bottom row). The performance increase from methods KX to Z01, and from methods Z01 to Z02 are both significant to the level $p < 0.01$ (Student's *t*-test for two paired samples).

The large number of tracking failures of methods KX [9], [15] and Z01 [13] can be traced back in most cases to either poor detection of pseudopods and the subsequent progressive breakdown of segmentation, or poor separations of cells in contact. In contrast, the small number of residual tracking failures of our method Z02 appears to occur in cases where cells interact so strongly with each other that no boundary is visible between cells. To handle these situations, it might be necessary in the future to include constraints of temporal (in addition to spatial) regularity into the segmentation process (see Section VI-B).

TABLE I
TRACKING PERFORMANCE COMPARISON OF THREE PARAMETRIC ACTIVE CONTOUR METHODS. THE TABULATED PERCENTAGES ARE THE 'TRACKING PERFORMANCE' RATIOS DEFINED IN THE TEXT. THE SIX TOP ROWS INDICATE RESULTS FOR EACH SEQUENCE. THE BOTTOM ROW INDICATES AVERAGES (AVG.) AND STANDARD DEVIATIONS (STD.) OVER ALL SEQUENCES

Image sequence	Tracking performance (%)		
	Method KX	Method Z01	Method Z02
a	29	57	100
b	70	80	100
c	31	60	94
d	41	45	91
e	50	79	86
f	47	80	100
avg. (std.)	**44.7 (15.0)**	**66.8 (14.9)**	**95.2 (5.9)**

In addition to evaluating the quantity of data extracted by our tracking method, it is also useful to assess the quality of these data. To do so, we compared the automatically computed cell positions to a manually obtained ground-truth. For each of the six sequences, four users U_i, $i = 1 \ldots 4$ were asked to track the positions of a cell by pointing on the perceived cell centers $\mathbf{r}_i$ on consecutive frames. (To limit the manual effort, the sequence of frames were decimated by a factor of ten, still allowing comfortable visual tracking of cellular identity.) A set of reference positions can then be computed by averaging the manually obtained positions among users. Instead of computing a single reference set by averaging all four $\mathbf{r}_i$, we performed a "leave-one-out" analysis. Therefore, we define four sets of reference points $\mathbf{R}_i = 1/3\Sigma_{j \neq i}\mathbf{r}_j$ obtained by excluding each user U_i in turn from the averaging. This allows us to compare both the automatically computed positions $\mathbf{r}_a$ (obtained as the mass

centers of the segmented regions) and the manual positions of each user U_i to the same reference points $\mathbf{R}_i$. For each user $i \in [1,4]$, each image and each target cell, thus, we compute the position error $\delta r_{a,i} = |\mathbf{r}_a - \mathbf{R}_i|$ of the automatic tracking and the position error $\delta r_{m,i} = |\mathbf{r}_i - \mathbf{R}_i|$ of the manual tracking method.

Table II indicates in nonbold numbers the mean and standard deviation of $\delta r_{a,i}$ (respectively, $\delta r_{m,i}$) for individual trial sequences (a)–(f) and individual references (respectively users). Bold numbers on every fifth row indicate averages over the four references/users, while the last five rows indicate averages over all sequences. With both manual and automatic tracking, the position errors are small compared to the size of the cells, which have an average effective diameter of roughly 40 pixels. For all sequences, the average "automatic" error $\delta r_{a,i}$ is smaller than the average manual error $\delta r_{m,i}$ of most users i (compare nonbold numbers in columns 3 and 5 of Table II), and the average automatic error is always smaller than the average manual error (see values for the "average user" $\bar{\mathbf{U}}$, obtained by averaging over all 4 users). Averaged over all trial sequences, the mean position errors of users U_1, U_2, U_3 and U_4 are, respectively, 3.97, 2.45, 3.23, and 3.56 pixels. The errors of the automatic method, determined using the same references as for the manual errors are slightly, but significantly smaller than those of users U_1, U_3 and U_4 (*t*-test for two paired samples: $p < 0.001$, $p < 0.002$, $p < 0.03$, respectively; relevant numbers are in columns 3 and 5 in the four top rows of the last group of five rows). The small unfavorable difference with user U_2 is only marginally significant ($p = 0.07$). The dispersion of errors of the automatic method, as reflected by the standard deviations, does not differ significantly from that of manual errors (compare columns 4 and 5) except for user U_1, who has greater error dispersion.

From these results, the automatic tracking can be considered to be at least as accurate, if not more accurate, than manual tracking. The small dispersion of the means and standard deviations of $\delta r_{a,i}$ among the four references (as compared to that of $\delta r_{m,i}$ among users), indicates that the reference positions are relatively robust to permutations of the users, therefore, these reference positions are likely to be good approximations of the true cell positions.

The position errors of the automatic method cannot be attributed to individual user errors and instead reflect imperfect segmentations. As previously mentioned, these errors are largest when cells are in strong interaction and the boundary between them becomes invisible. A significant further reduction in positioning error could be achieved by improving segmentation for these situations (see Section VI-B).

TABLE II
COMPARISON OF AUTOMATIC AND MANUAL TRACKING. TABULATED VALUES ARE THE AVERAGE (AVG.) AND STANDARD DEVIATION (STD.) OF POSITION ERRORS FROM AUTOMATIC ($\delta r_{a,i}$) OR MANUAL ($\delta r_{m,i}$) TRACKING COMPARED TO THE REFERENCE POSITIONS. FOR A GIVEN USER, THE REFERENCE POSITIONS ARE OBTAINED BY AVERAGING THE POSITIONS DEFINED BY THE OTHER THREE USERS. AVERAGES OVER THE FOUR REFERENCES/USERS ARE GIVEN IN BOLD ON EVERY FIFTH ROW. THE LAST FIVE ROWS INDICATE AVERAGES OVER ALL TRIAL SEQUENCES. ALL VALUES ARE IN PIXELS

Image sequence	User U_i	Position errors (pixels)			
		Automatic ($\delta r_{a,i}$)		User U_i ($\delta r_{m,i}$)	
		avg.	std.	avg.	std.
a	U_1	2.24	1.64	3.50	1.93
	U_2	2.25	1.54	2.27	1.28
	U_3	2.29	1.64	2.50	1.53
	U_4	2.28	1.53	2.13	1.30
	$\bar{\mathbf{U}}$	**2.26**	**1.59**	**2.60**	**1.51**
b	U_1	2.12	1.27	3.27	1.87
	U_2	2.37	1.33	2.05	1.17
	U_3	2.60	1.43	3.30	1.71
	U_4	2.41	1.30	3.98	1.85
	$\bar{\mathbf{U}}$	**2.37**	**1.33**	**3.15**	**1.65**
c	U_1	2.76	1.42	3.67	2.18
	U_2	2.85	1.44	2.30	1.41
	U_3	2.69	1.47	3.32	1.76
	U_4	2.92	1.56	3.49	1.83
	$\bar{\mathbf{U}}$	**2.80**	**1.47**	**3.19**	**1.79**
d	U_1	2.66	1.63	4.49	2.54
	U_2	2.90	1.68	2.79	1.84
	U_3	2.92	1.73	3.35	1.96
	U_4	3.20	1.74	4.13	2.23
	$\bar{\mathbf{U}}$	**2.92**	**1.69**	**3.69**	**2.14**
e	U_1	2.69	2.14	4.60	2.76
	U_2	3.14	2.09	2.70	1.62
	U_3	2.90	2.13	3.66	1.81
	U_4	3.29	2.07	3.79	1.98
	$\bar{\mathbf{U}}$	**3.00**	**2.11**	**3.69**	**2.04**
f	U_1	2.20	1.40	4.27	2.67
	U_2	2.55	1.59	2.57	1.39
	U_3	2.50	1.51	3.27	1.81
	U_4	2.52	1.64	3.85	2.13
	$\bar{\mathbf{U}}$	**2.44**	**1.53**	**3.49**	**2.00**
avg.	U_1	**2.44**	**1.58**	**3.97**	**2.30**
	U_2	**2.68**	**1.61**	**2.45**	**1.45**
	U_3	**2.65**	**1.65**	**3.23**	**1.76**
	U_4	**2.77**	**1.60**	**3.56**	**1.89**
	$\bar{\mathbf{U}}$	**2.63**	**1.62**	**3.30**	**1.86**

C. Applications

The segmentation and tracking method presented here is designed to allow the quantitative analysis of cellular shape and motion from videomicroscopy data. We have applied our tool in a biological research project [21] to compare the motility of different strains of *E. histolytica*. The automatic tracking of a large number of cells was instrumental in enabling statistically significant comparisons of motility between strains despite the important dispersion of the motility phenotype within each strain [21]. In future studies, we will apply our method to quantitatively analyze the dynamics of cellular morphology. The results of such analyzes should help in selecting molecules targeting the parasite's potential for invasion and paghocytosis, and thereby reducing its pathogenicity.

VI. CONCLUSION

A. Summary

We have presented a quasi-automatic method to track and segment highly deformable cells through large image sequences based on the framework of parametric active contours [9] (Section II-A). Our method uses the GVF model [15] (Section II-B) to increase segmentation robustness, topological operators [20] (Section IV-B) to handle cell divisions, and introduces the new concept of repulsive interactions between contours to handle

cell contacts. The proposed techniques largely overcome two main shortcomings of previously reported approaches in their application to cellular imaging, namely their inability to correctly segment pseudopods and cells in contact. To achieve correct segmentation of pseudopods, we used an edge map that takes advantage of the relative homogeneity of the background to better localize weak object boundaries (Section III). To maintain contour separation between objects in contact, and allow correct localization of this separation at the cell-cell interface, we integrated a repulsive coupling between contours into the energy minimization scheme through a modification of the local edge map (Section IV-C). The ability of our method to substantially improve cell tracking was demonstrated experimentally on a representative data set (Section V-B).

Our approach will be useful to quantitatively study the dynamics of various migrating cells such as amoeba, fibroblasts, leukocytes, or tumor cells. It could thereby find applications in the fields of tissue repair, inflammatory response and cancer, as well as for studies of non pathogenic processes such as embryonic development.

B. Future Work

Additional efforts will be required to overcome some of the limitations of the present technique.

- Our method only tracks the cells that were manually initialized in the first frame, and is unable to handle objects entering the scene later in the sequence. In the applications of our method, we bypassed this issue at the expense of the extracted amount of data, by confining our study to cells remaining in the field of view throughout the sequence. To take full advantage of the whole data set, the proposed framework should be supplemented by an automatic initialization scheme at the borders of the field of view, aiming at detecting new objects. This might be done by a limited use of the level-set technique [17].
- The integration of region statistics into an active contour approach (e.g., [22]) potentially offers higher robustness to image noise and may be applicable to a wider range of image modalities.
- Occasionally, cells interact so closely that any boundary between them becomes invisible, and in experiments requiring a large density of cells, objects may be in such close contact that the background can no longer be used for the segmentation. To handle these cases, it may be necessary to impose temporal continuity constraints to establish object identities and boundaries. This might be achieved within the framework of deformable models [4] by considering the $2D + T$ image sequence as a three-dimensional data set.

ACKNOWLEDGMENT

The authors would like to thank the two referees for their careful reviews and suggestions, which led to substantial improvements of this manuscript. They are grateful to E. Glory, A. Genevesio, and M. Féral for their devoted help with the tedious task of manual tracking. They also thank G. Stamon for his constant encouragement.

REFERENCES

[1] D. A. Lauffenburger and A. F. Horwitz, "Cell migration: A physically integrated process," *Cell*, vol. 84, pp. 359–369, 1996.
[2] M. Chicurel, "Cell migration research is on the move," *Science*, vol. 295, pp. 606–609, 2002.
[3] A. Roumier, J.-C. Olivo-Marin, M. Arpin, F. Michel, P. Mangeat, O. Acuto, A. Dautry-Varsat, and A. Alcover, "The membrane-microfilament linker ezrin is involved in the formation of the immunological synapse and in T cell activation," *Immunity*, vol. 15, pp. 715–728, 2001.
[4] T. McInerney and D. Terzopoulos, "Deformable models," in *Handbook of Medical Imaging*, I. N. Bankman, Ed. New York: Academic, 2000, pp. 127–145.
[5] T. D. Jones and P. Plassmann, "An active contour model for measuring the area of leg ulcers," *IEEE Trans. Med. Imag.*, vol. 19, pp. 1202–1210, Dec. 2000.
[6] T. Kirubarajan, Y. Bar-Shalom, and K. R. Pattipati, "Multiassignment for tracking a large number of overlapping objects," in *Multitarget-Multisensor Tracking: Applications and Advances*, Y. Bar-Shalom and W. D. Blair, Eds. Norwood, MA: Artech House, 2000, vol. III, pp. 199–231.
[7] P. Arhets, J.-C. Olivo, P. Gounon, P. Sansonetti, and N. Guillèn, "Virulence and functions of myosin II are inhibited by overexpression of light meromyosin in *Entamoeba histolytica*," *Mol. Biol. Cell.*, vol. 8, pp. 1537–1547, 1998.
[8] M. J. Brown and L. M. Loew, "Electric field-directed fibroblast locomotion involves cell surface molecular reorganization and is calcium dependent," *J. Cell Biol.*, vol. 127, no. 1, pp. 117–128, 1994.
[9] M. Kass, A. Witkin, and D. Terzopoulos, "Snakes: Active contour models," *Int. J. Comput. Vision*, vol. 1, pp. 321–331, 1988.
[10] F. Leymarie and M. D. Levine, "Tracking deformable objects in the plane using an active contour model," *IEEE Trans. Pattern Anal. Machine Intell.*, vol. 15, pp. 617–634, June 1993.
[11] K. A. Giuliano, R. DeBiasio, P. Feineigle, and D. L. Taylor, "Toward the automated dissection of morphological and molecular dynamics of living normal and transformed cells," in *Motion Analysis of Living Cells*, D. R. Soll and D. Wessels, Eds. New York: Wiley, 1998, pp. 53–65.
[12] V. Meas-Yedid and J.-C. Olivo-Marin, "Active contours for the movement and motility analysis of biological objects," *Proc. IEEE Int. Conf. Image Processing*, vol. 1, pp. 196–199, 2000.
[13] C. Zimmer, V. Meas-Yedid, E. Glory, E. Labruyère, N. Guillén, and J.-C. Olivo-Marin, "Active contours applied to the shape and motion analysis of amoeba," in *Proc. SPIE's 46th Annual Meeting, Vision Geometry X*, vol. 4476, 2001, pp. 124–134.
[14] D. Bray, *Cell Movements*. New York: Garland, 1992.
[15] C. Xu and J. L. Prince, "Snakes, shapes, and gradient vector flow," *IEEE Trans. Image Processing*, vol. 7, pp. 359–369, Mar. 1998.
[16] J. F. Canny, "A computational approach to edge detection," *IEEE Trans. Pattern Anal. Machine Intell.*, vol. PAMI-8, pp. 679–698, June 1986.
[17] J. A. Sethian, *Level Set Methods and Fast Marching Methods*. Cambridge, U.K.: Cambridge Univ. Press, 1999.
[18] T. F. Chan and L. A. Vese, "Active contours without edges," *IEEE Trans. Image Processing*, vol. 10, pp. 266–277, Feb. 2001.
[19] A. Tsai, A. Yezzi, and A. S. Willsky, "Curve evolution implementation of the Mumford-Shah functional for image segmentation, denoising, interpolation, and magnification," *IEEE Trans. Image Processing*, vol. 10, pp. 1169–1186, Aug. 2001.
[20] H. Delingette and J. Montagnat, "Shape and topology constraints on parametric active contours," *Comput. Vision Image Understand.*, vol. 83, pp. 140–171, 2001.
[21] E. Labruyère, C. Zimmer, V. Galy, J.-C. Olivo-Marin, and N. Guillén, "Control of *Entamoeba histolytica* polarity and migration by an original member of the p21-activated kinase family, EhPAK," *J. Cell Sci.*, vol. 116, pp. 61–71, 2003.
[22] S. C. Zhu and A. Yuille, "Region competition: Unifying snakes, region growing and bayes/MDL for multiband image segmentation," *IEEE Trans. Pattern Anal. Machine Intell.*, vol. 18, pp. 884–900, Sept. 1996.